JCIM JOURNAL OF CHEMICAL INFORMATION AND MODELING

pubs.acs.org/jcim Article

Omicron Binding Mode: Contact Analysis and Dynamics of the Omicron Receptor-Binding Domain in Complex with ACE2

Zsolt Fazekas, Dóra K. Menyhárd, and András Perczel*

Cite This: https://doi.org/10.1021/acs.jcim.2c00397 Read Online

ACCESS | Metrics & More | Article Recommendations | Supporting Information

ABSTRACT: On 26 November 2021, the WHO classified the Omicron variant of the SARS-CoV-2 virus (B.1.1.529 lineage) as a variant of concern (VOC) (*COVID-19 Variant Data, Department of Health,* 2022). The Omicron variant contains as many as 26 unique mutations of effects not yet determined (Venkatakrishnan, A., *Open Science Framework,* 2021). Out of its total of 34 Spike protein mutations, 15 are located on the receptor-binding domain (S-RBD) (*Stanford Coronavirus Antiviral & Resistance Database,* 2022) that directly contacts the angiotensin-converting enzyme 2 (ACE2) host receptor and is also a primary target for antibodies. Here, we studied the binding mode of the S-RBD domain of the Spike protein carrying the Omicron mutations and the globular domain of human ACE2 using molecular dynamics (MD) simulations. We identified new and key Omicron-specific interactions such as R^{493} (of mutation Q493R), which forms salt bridges both with E^{35} and D^{38} of ACE2, Y^{501} (N501Y), which forms an edge-to-face aromatic interaction with Y^{41}, and Y^{505} (Y505H), which makes an H-bond with E^{37} and K^{353}. The glycan chains of ACE2 also bind differently in the WT and Omicron variants in response to different charge distributions on the surface of Spike proteins. However, while the Omicron mutations considerably improve the overall electrostatic fit of the two interfaces, the total number of specific and favorable interactions between the two does not increase. The dynamics of the complexes are highly affected too, making the Omicron S-RBD:ACE2 complex more rigid; the two main interaction sites, Patches I and II, isolated in the WT complex, become connected in the Omicron complex through the alternating interaction of R^{493} and R^{498} with E^{35} and D^{38}.

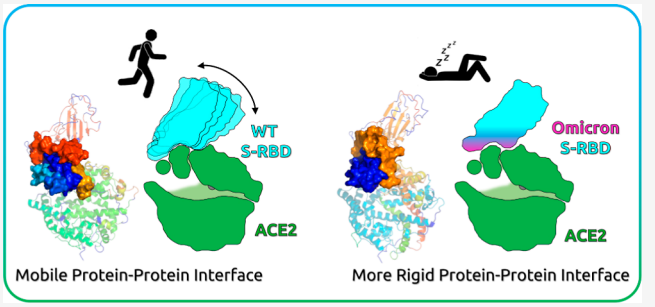

1. INTRODUCTION

Due to an unprecedented,[1−3] focused effort of the scientific community, much has been discovered concerning the host invasion and replication cycle of SARS-CoV-2 coronaviruses.[4−11] Since the outbreak of the COVID-19 pandemic (officially classified as such in March of 2020),[12] there has been a large diversification of the SARS-CoV-2 viral genome circulating worldwide. The most notable variants to date [Variants of Concern (VOCs)], B.1.1.7 Alpha, B.1.351 Beta, P.1 Gamma, and B.1.617.2 Delta variants,[13−15] carried a moderate number of amino acid changes as compared to the original Wuhan variant. However, in the currently dominant B.1.1.529 Omicron virus, 50 non-synonymous mutations were identified. The virus Spike protein, responsible for host receptor recognition, carries 34 mutations, 15 of which are located on the receptor-binding domain (S-RBD), the outermost interacting edge of the Spike protein, which resulted in an unparalleled increase in the infection rate and immune evasion. However, somewhat unexpectedly, the Omicron mutations also reduced the effectiveness of Spike protein cleavage by furin (one of the key steps of the Spike-activation cascade) and of cell−cell fusion,[16,17] also demonstrating a greatly varied effect on the efficiency of cell invasion of different cell lines.[16−19] Overall, the mutations seem to have created a virus that poses less severe clinical implications than the previous Delta variant.[20] Omicron is the first VOC wherein infectivity and virulence are so clearly decoupled that it underlines the need for a yet more detailed understanding of the mechanisms involved in host invasion by SARS-CoV-2.

The human angiotensin-converting enzyme 2 (ACE2) has been recognized as the most important receptor of SARS-CoV-2;[21−23] thus the structure and strength of the Spike:ACE2 complex is considered one of the major determinants of viral infectivity and symptom development (Figure 1). However, thus far, markedly contradicting experimental results have emerged concerning the effectiveness of the Spike:ACE2 interaction in the case of the Omicron variant,[17,24−28] ranging between 3-fold increase and 15-fold decrease in affinity as compared to that of the original Wuhan form (WT).

The cryoelectron microscopy (cryo-EM)-derived and crystal structure of the wild-type Spike RBD (WT S-RBD):ACE2 complex was solved (PDB ID: 6M17 and 6M0J),[29,30] which showed an ∼900 Å^2 buried surface area upon complexation. The interaction surface, from the Spike protein's side, consists of three loops[31,32] (those of 474−485, 488−490, and 494−

Received: April 7, 2022

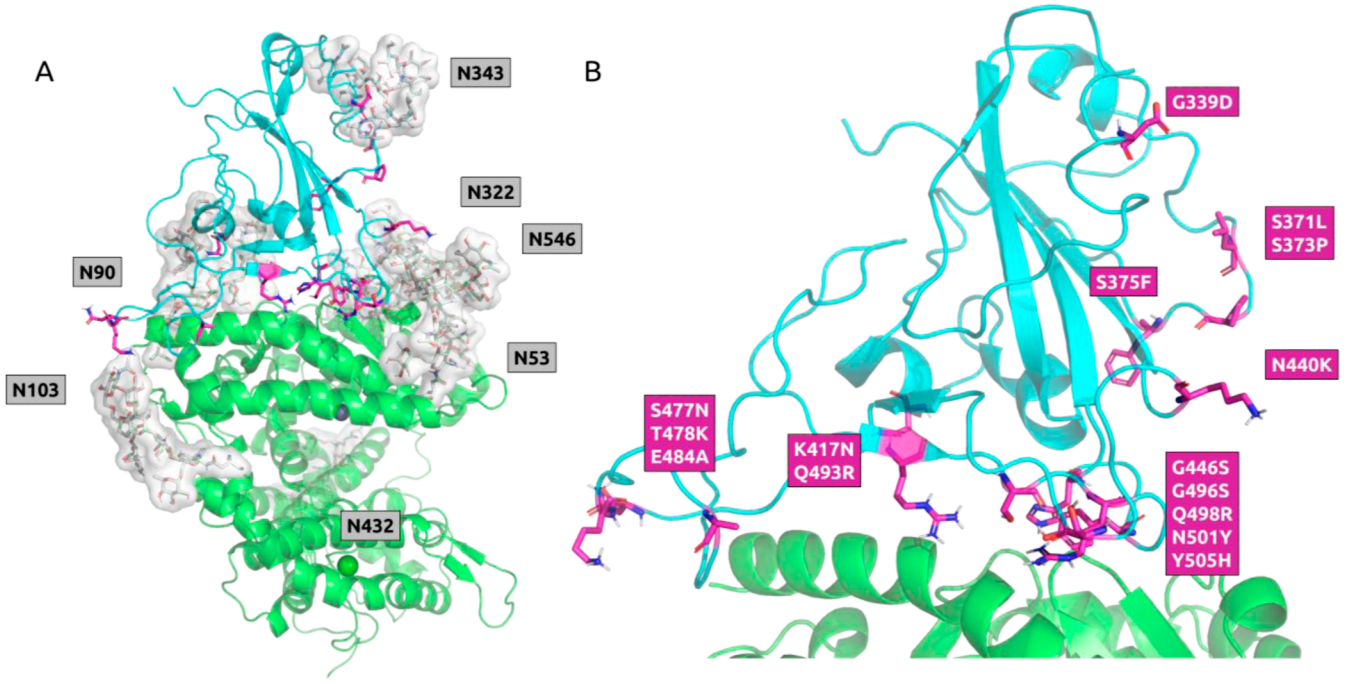

Figure 1. (A) Structures of the Omicron S-RBD domain (cyan) bound to ACE2 protein (green) and all the seven glycoantennas associated (gray) with it. (B) All the 15 Omicron S-RBD specific mutation sites are depicted (magenta), of which 10 are located at the interface.

505) along with nearby supporting residues, which face the first two helices and the neighboring residues of ACE2 in the complex. The mobile loops, constituting the receptor binding motif of the S-RBD, are stabilized when bound to ACE2, forming several intermolecular H-bonds (Y^{449}, Q^{492}, and Q^{498}), hydrophobic interactions (Y^{473}, A^{475}, and F^{486}), and salt bridges (K^{417}). No less than 10 of the 15 Omicron S-RBD mutations are located on this interface constituting nearly half of the interacting residues, suggesting that both conformation and dynamics might be largely affected by the changes.

Recently, both cryo-EM-derived and crystal structures of the Omicron S-RBD:ACE2 complex were also deposited into the PDB (ID: 7T9L,[33] 7WBP and 7WBL[27]), highlighting several changes in the interface. The relatively similar structures (the backbone trace of the interaction surfaces (see Materials and Methods) can be fitted with a root-mean-square deviation (RMSD) of 0.46−0.73 Å), show an extensive H-bonding network comprising D^{38}, Q^{42}, and K^{353} from the ACE2 side and Y^{449}, S^{496}, Y^{501}, and G^{502} from the S-RBD side. Besides this, H-bonds are present between H^{34}-Y^{453}, E^{35}-R^{493}, Y^{41}-T^{500}, and Y^{83}-N^{487}, along with a hydrophobic cluster created by F^{28}, L^{79}, M^{82}, and Y^{83} in ACE2 and F^{486} in S-RBD. Two other smaller networks are formed between K^{353} from the ACE2 side and G^{496} and G^{502} from the S-RBD side and also between Q^{24} and Y^{83} from the ACE2 side and N^{487} from the S-RBD side. An H-bond between Y^{41}-T^{500} and a salt bridge between D^{30}-K^{417} are also present.

As both the Spike and ACE2 are glycoproteins[34] (contributing significantly to the immune evasion[35] of the former in the vicinity of the latter), it is important to consider the effects of the glycan-conjugated side chains at the glycosylation sites. The extracellular domain of ACE2 has seven *N*-glycosylation sites, namely, N^{53}, N^{90}, N^{103}, N^{322}, N^{432}, N^{546}, and N^{690}, out of which N^{53}, N^{90}, N^{103}, and N^{322} are all capable of interacting with the S-RBD within the complex. In contrast, the S-RBD has only one glycosylation site, that of N^{343}, approximately 26 Å away from the interface. It has been reported that these glycosylated residues can both enhance[36,37] (ACE2 N^{322}) or weaken (ACE2 N^{90}) the interaction between the two proteins.[38] Due to the large number of mutations on the Omicron RBD and the number and relative size of these glycan modifications, it can be expected that the mutated residues exert some kind of effect on the glycans and vice versa. However, in the cryo-EM and crystal structures, these glycan modifications are only partly visible due to their highly mobile nature.

Here, we carried out molecular dynamics (MD) simulations to assess the structural and dynamic effects of the Omicron mutations on the S-RBD:ACE2 complex, using fully glycosylated models of both the WT and mutant variants (Figure 1). Such MD simulations have been proved useful for clarifying the molecular details of the viral behavior.[39−43] We found that while the Omicron mutations create a favorable change in overall electrostatics, the S-RBD:ACE2 complex is not strengthened due to steric uncomplementarity at the crowded interaction surface. We also found that the dynamics of the complex is altered by the Omicron mutations. Through an anchoring H-bond network—located in the middle of the interaction surface, connecting the two previously recognized hot spots, Patches I and II—the Omicron complex interface becomes more rigid, suggesting a larger loss in degrees of freedom and unfavorable $\Delta\Delta_{bind}S$.

2. RESIDUE-SPECIFIC INTERACTIONS

To obtain directly comparable results, both simulations were started from the crystal structure of the WT S-RBD:ACE2 complex (PDB ID: 6M17),[30] introducing the Omicron mutations manually without changing the backbone structure of the complex. The obtained equilibrium ensemble of the two states shows appreciable similarity to the experimentally determined structures of the corresponding complexes (with an RMSD of 1.43 Å for the backbone trace of the interaction

https://doi.org/10.1021/acs.jcim.2c00397
J. Chem. Inf. Model. XXXX, XXX, XXX−XXX

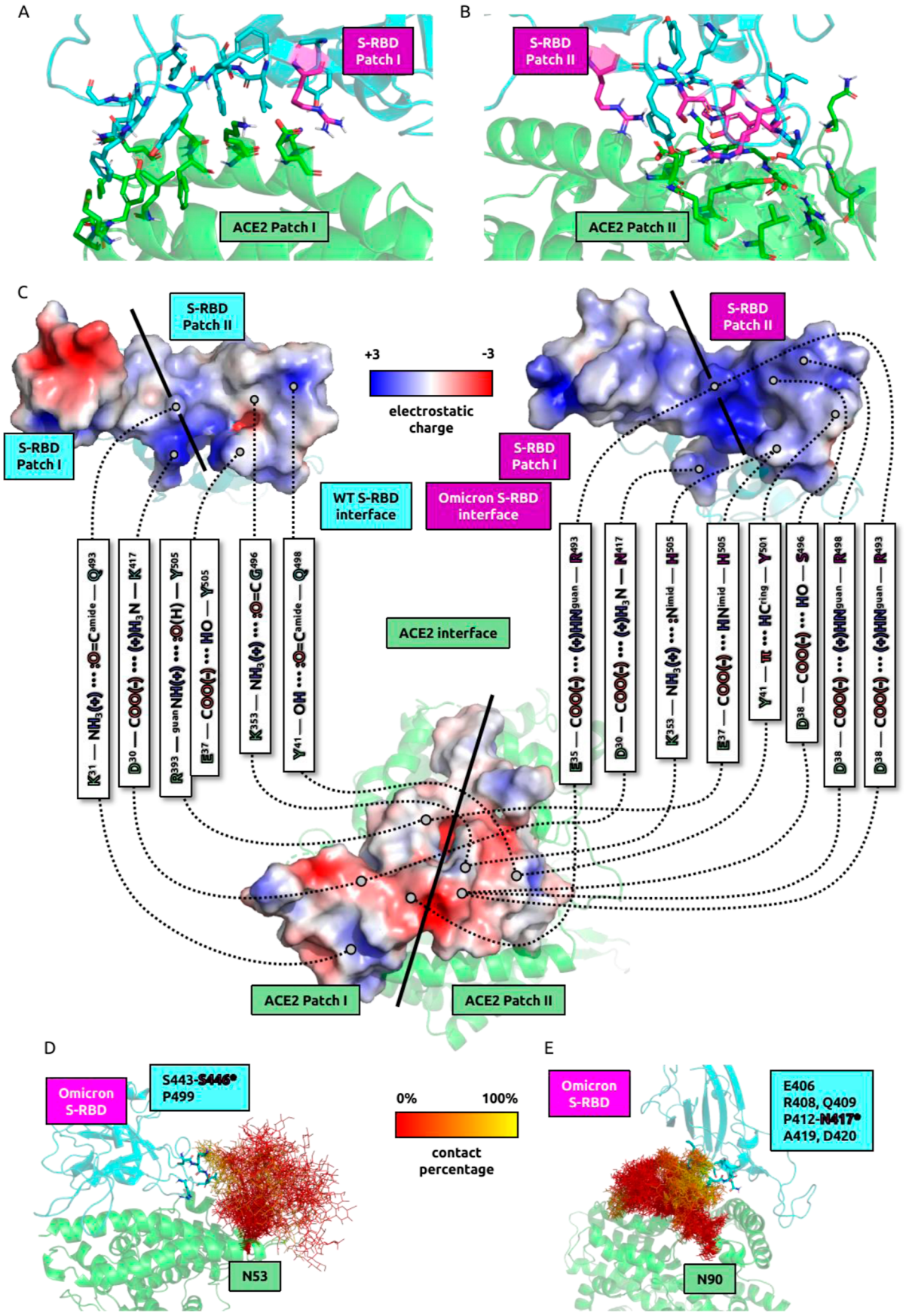

Figure 2. Patches I (A) and II (B) of the Omicron S-RBD:ACE2 interaction surface (shown on the central structure of the most populated cluster of the MD simulation). Patch I consists of residues 21−35 in H1, and residues 79−84, present in the C-terminal part of helix 2 (H2, residues 56−84) of ACE2, and 453−456, 473−476, and 485−493 of S-RBD. Patch II comprises the 37−45 (part of H1) and 353−357 segments, along with

https://doi.org/10.1021/acs.jcim.2c00397
J. Chem. Inf. Model. XXXX, XXX, XXX−XXX

Figure 2. continued

N^{330} of ACE2, and residues 493−505 of S-RBD, along with Y^{449}. Mutation sites are highlighted with magenta. It can be seen that R^{493} can interact with both Patch I and Patch II residues (mostly with E^{35} and D^{38}). (C) Poisson−Boltzmann electrostatic surfaces of the WT S-RBD interface, the Omicron S-RBD interface, and the ACE2 interface. The surfaces are color-coded with a blue-white-red spectrum ranging from charge +3 to −3. Residue−residue interactions are denoted by dashed lines and their corresponding text-boxes. Patches are separated with tilted, bold lines also indicating their mode of superposition on ACE2. (D,E) Glycan ensembles of N^{53} and N^{90}, respectively. The glycan-atoms are color-coded with a red-yellow spectrum, ranging from 0 to 100% according to their contact frequencies with the corresponding glycan's S-RBD contact residues.

surfaces of the two proteins when the WT calculated ensemble and the cryo-EM structure of 6M17 is compared, and 1.41 Å, 1.45 Å, and 1.33 Å for the same atom set of the calculated model set of the Omicron variant:ACE2 complex when compared to structures 7WBP, 7WBL, and 7T9L, respectively), which is especially significant in the case of the simulation concerning the Omicron variant, which achieved this degree of similarity despite being initiated from the structure of the WT-ACE2 complex.

Residue−residue contacts of the key interacting residue pairs of the simulated WT and Omicron RBD:ACE2 complexes are compared in Figures S5−S11. From a global perspective, the interface of the Omicron S-RBD becomes more positively charged, when compared to its WT counterpart. The E484A mutation diminishes a negative charge, while the T478K, Q493R, and Q498R mutations introduce positive charges at the interface, overall (also including the opposing effects of K417N and N440K mutations) a +4 electrostatic change is acquired. These alterations could have occurred to enhance the electrostatic attraction toward the ACE2 interface, which is predominantly negatively charged. The ACE2 helix 1 (H1, residues between 21-52) contains six negatively charged and only two positively charged residues, making it highly negative and therefore more easily targeted by the Omicron S-RBD interface (Figures 2/c, S12−S14).

The interacting residues of the two proteins can be divided into two independent hot spots at either end of the contact surface—Patches I and II (following the nomenclature of Yin et al.[33])—separated by a segment along which no specific interaction is formed, as in the case of the WT S-RBD:ACE2 complex (Figure 2/A,B).

The Q493R Omicron mutation occurs at this critical spot and determines the flexibility of both Patch I and II contacts. The WT Q^{493} residue interacts with K^{31} and E^{35}, both within Patch I, in an anticorrelated manner. In fact, the Spearman correlation coefficient (SpR) between the Q^{493}-K^{31} and the Q^{493}-E^{35} interaction distance is −0.39. In the Omicron variant, R^{493} changes interaction partners: instead of contacting K^{31}, it forms salt bridges with E^{35} in 70% of the time and with D^{38} in 30% of the time. In contrast to the WT, the SpR coefficient changes to −0.54 in the case of the R^{493}-E^{35} and the R^{493}-D^{38} distance pairs, making these distances more dependent on each other. Considering all this, upon the Q493R mutation, a solitary Patch I interaction (Q^{493}-K^{31}, E^{35}) is replaced by an alternating bidentate E^{35}-R^{493}-D^{38} salt bridge network, linking Patch I and Patch II through the newly introduced guanidino group. This can partly restrict the movement of the S-RBD interface with respect to H1. Interestingly, when comparing the crystal and cryo-EM structures of the of Omicron S-RBD:ACE2 complex (7WBP, 7WBL—neither of which is of sufficiently high resolution that would allow unequivocal assignation of sidechain conformations), it is this region that shows the greatest differences—with H^{34}, D^{38}, and R^{493} in characteristically different conformations in the two. Thus, the multistate nature of this interaction hot spot is reflected in the experimental results too.

In the case of the Q498R mutation, again, a solitary Patch II interaction (Q^{498}-Y^{41}) is replaced by a loosely correlated bifurcated interaction (D^{38}-R^{498}-Q^{42}), where the distance SpR is 0.34. However, because D^{38} already participates in a salt bridge with R^{493}, the R^{498}-D^{38} interaction only occurs in about 22% of the time. The distance SpR between R^{493}-D^{38} and R^{498}-D^{38} is −0.02, indicating that these distances can change independently of another. Nevertheless, this interaction further extends the anchoring of the Patches.

The N501Y change replaces a H-bond with Y^{41} of the WT S-RBD:ACE2 complex with a fixed σ-π interaction in the Omicron variant. This way, the partially polarized $C^{\varepsilon}(\delta-)$−$H(\delta+)$ bond of Y^{501} can interact with the negatively charged π electron cloud of Y^{41}. This mutation is also present in the Alpha, Beta, Gamma, and Mu variants[3] and is considered stabilizing.[44−46] The Y505H mutation, which has not been observed before, replaces a stable Y^{505}-R^{393} H-bond and a partial Y^{505}-E^{37} H-bond of the WT complex with the H^{505}-E^{37} and H^{505}-K^{353} H-bond. These interactions are highly anticorrelated with a SpR of −0.72.

Interestingly, not all Omicron mutations lead to improvement of the local interaction network. In the WT complex, the S-RBD N^{440} and G^{446} interact with N^{53} and Q^{42}, respectively, while within the Omicron complex the mutated residues K^{440} and S^{446} make no contacts with these or any other residues of ACE2. Overall, in the central region of the interaction surface, the introduction of the Omicron mutations fortifies the interchain contacts, but it also shifts the distribution of the total number of interchain H-bonds (at each snapshot), decreasing the average from 10.7 (SD: 2.2) seen in the case of the WT complex to 9.9 (SD: 1.9) (Figure S17). In order to assess the binding free energy difference of the two systems, we used the EMBL-EBI PISA server to estimate the solvation free energy gain upon formation of the complexes (see the Materials and Methods section). For the WT complex, this resulted in a −8.1 kcal/mol value (SD: 1.3 kcal/mol), while for the Omicron mutant complex this resulted in a less favorable value of −6.2 kcal/mol (SD: 1.3 kcal/mol).

3. GLYCAN-SPECIFIC INTERACTIONS

Both the S-RBD and the ACE2 contain *N*-glycosylation sites. Some of the glycan modifications at these sites are sufficiently long to directly interact with the other protein partner and cause differences in the binding mode and dynamics. These modifications show microheterogenicity, thus for the simulations we considered the most abundant glycan modification at each site[47] (Figure S15).

Geometrically, the glycans at positions 53, 90, 103, and 322 on the ACE2 and 343 on the S-RBD are the ones capable of interacting with residues and glycans from the other chain. Despite this, only the N^{53}, N^{90}, and N^{103} ACE2 glycans form contacts with the S-RBD. The glycan at N^{322} of the Spike is

https://doi.org/10.1021/acs.jcim.2c00397
J. Chem. Inf. Model. XXXX, XXX, XXX−XXX

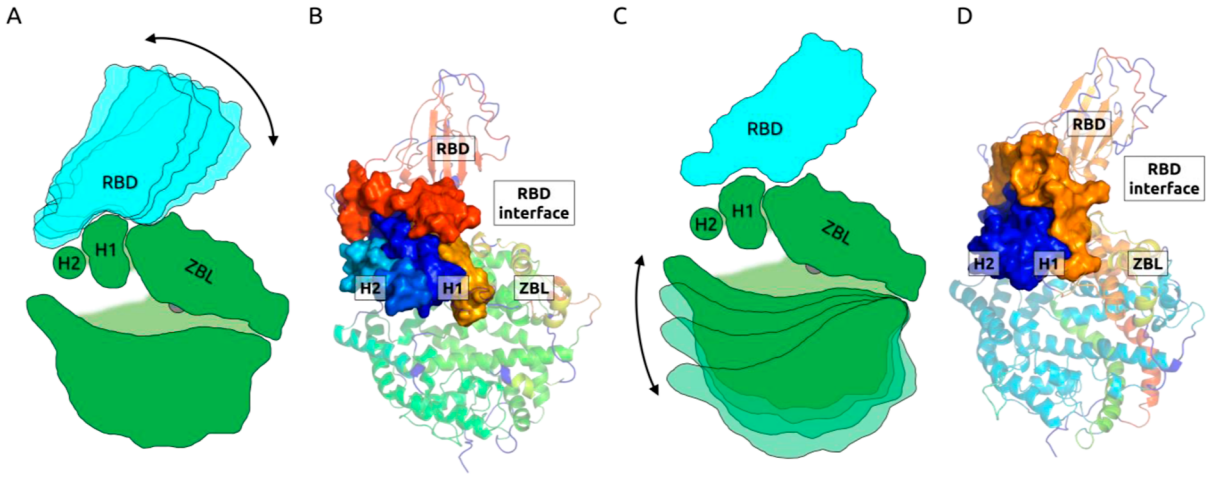

Figure 3. PCA and rigid body segmentation of the WT and the Omicron complexes. Panels A and C show the movement of the WT and the Omicron complexes along the first principal axis, respectively. While the WT S-RBD interface can move relatively freely on H1 in a sliding manner, this type of movement cannot be observed for the Omicron complex. This difference in interface dynamics is also apparent when the structures are segmented into rigid parts, shown in panel (B) for the WT, and (D) for the Omicron complex. In the case of the WT complex, the interface is segmented into five different rigid parts (shown as five differently colored surfaces), indicating several mobile elements, while the Omicron interface is segmented into two rigid parts only.

bound to the homochain N^{546} glycan in both considered systems, keeping it away from the S-RBD residues. The N^{343} glycan on the S-RBD also forms homochain contacts, far (residues 364−371) from the S-RBD:ACE2 interface.

The glycan N^{103} of ACE2 only shows contact with two residues from the S-RBD, namely F^{486} and N^{487} in the Omicron complex, and no contacts in the WT complex. In the case of N^{53}, we obtained similar results for the WT and the Omicron S-RBD:ACE2 complex. The common contacting amino acids are S^{443}, K^{444}, V^{445}, and P^{499}. The residues N^{439}, N^{440}, L^{441}, D^{442}, and Q^{498} only contact with N^{53} in the WT complex, while S^{446} only contacts in the case of the Omicron complex, slightly differentiating the behavior of this glycan in the two cases. The main contacting sugar subunit is the terminal *N*-acetyl glucosamine (NAcGlc) on the C^6-branch of the central mannose subunit. The C^3−OH and C^4−OH groups of this NAcGlc are closer than 4.0 Å to the contacting residues for the whole length of the trajectory examined, forming H-bonds with the amide groups of these residues.

The glycan chains of N^{90} behave radically different in the two complexes; they share only one common contacting residue, namely D^{420}, and bind to different patches on the S-RBD. Since in our simulation this glycan contains a sialic acid subunit, which is present in a deprotonated form, the large change in the S-RBD electrostatics possibly resulted in the relocation of its binding region. In the WT complex, it is bound to D^{420}-Y^{421}, F^{456}-R^{457}, S^{459}-L^{461}, I^{472}-G^{476}, and C^{480}, and its main contacting sugar subunits are ones on the C^3-branch, that is, the ones terminating in the sialic acid moiety. These contacts are realized through H-bonds of the sugar OH-groups and the *N*-acetyl groups of the NAcGlc and sialic acid, but not through the negatively charged carboxylate, which faces toward the bulk solvent. In contrast, in the Omicron complex, the N^{90}-glycan of ACE2 binds to the residues R^{408}-Q^{409}, P^{412}-N^{417}, A^{419}, and D^{420} of the Spike-protein. While in the WT complex, only the C^3-branch contacted with the S-RBD, in this case both the C^3- and the C^6-branches remain proximal to these residues. The subunits responsible for these contacts are the sialic acid (from the C^3-branch) and the terminal galactose (from the C^6-branch). Besides the typical sugar−OH...O=C−residue and sugar−(H)O...HN−residue interactions, the carboxylate of the sialic acid forms a H-bond with Q^{414} in one of the trajectories and also stays close to R^{408}, although it does not make a direct contact with it. In the other trajectory, the sialic acid moiety participates in intrachain interactions around the residues Q^{552}, N^{556}, and R^{559} of the Spike protein.

4. GLOBAL DYNAMICS

For the analysis of the complexes' global movements, first we applied principal component analysis (PCA) along the trajectory structures. A schematic representation of the first three principal movements for the WT and the Omicron complex can be seen in Figures 3 and S19.

Movement along the first principal axis in the WT complex results in a sliding/rocking motion of the S-RBD interface on the ACE2 interface. While a large portion (residues 497−505) of the S-RBD Patch II moves in unison with the ACE2 interface, Patch I rotates toward H2 with H1 as its axis of rotation. This indicates that Patch I is a loosely bound interface compared to Patch II. In the movements along the second and third principal axes, we cannot observe such uncorrelated motion between the S-RBD and the ACE2 side interfaces, that is, the motions of the S-RBD patches are highly correlated with the motions of the ACE2 patches. In contrast, the Omicron complex shows a different movement pattern. In the first principal movement, the whole interface of the S-RBD as well as the Patch II side of the ACE2 interface, with H^{34} and E^{35} from Patch I, move together without much internal deformation. This movement is mainly dominated by the opening−closing behavior of the ACE2 enzymatic active site. During the motion along the second principal axis, the whole RBD rotates around an axis perpendicular to the plane of the interface, which remains fairly rigid, while in the third principal motion a deformative motion occurs, in which the Patch I part of the S-RBD moves together with the *N*-terminal of H1 with Patch II remaining relatively motionless.

In order to segment the whole complex into parts that stay approximately undeformed along the trajectory, we calculated

https://doi.org/10.1021/acs.jcim.2c00397
J. Chem. Inf. Model. XXXX, XXX, XXX−XXX

the RMSD of each Cα−Cα distance, measured with respect to its average distance. This RMSD matrix was then used in a DBSCAN[48] clustering algorithm as a precomputed metric to segment the protein into parts, whose internal elements (Cα atoms) show a small distance variance (Figure 3).

In the case of the WT complex, this resulted in 18 clusters (counting the outliers, as a cluster). The full S-RBD interface aggregates into one cluster, while the ACE2 interface is segmented into four different clusters: the whole H1 and its connector loop (residues 21−54), the *N*-terminal part of H2 (residues 55−63), the C-terminal part of H2 (residues 65−82), and the antiparallel β-strand pair containing the hotspot K^{353} (residues 345−360). The fact that the whole interface is segmented into five relatively large parts suggests a dynamically changing interchain residue-interaction environment. In contrast, in the case of the Omicron complex (17 clusters in total), the interface is segmented into two parts only; one containing the full S-RBD interface, as well as the aforementioned β-strand pair, and another containing both H1 and H2 of ACE2. Because we used the same DBSCAN parameters for both runs, these results suggest differences in the dynamics of the two complex interfaces.

The two complexes also differ in their relative interface mobilities; we calculated the root mean squared fluctuations (RMSFs) for each atom and compared the median value of the ACE2-contacting S-RBD residues' backbone RMSF to the full backbone median RMSF. In the case of the WT complex, the mobility of the interface is 11% higher than the average full backbone mobility, whereas the interface of the Omicron complex is 9% less mobile than the average of the full backbone. This tendency can also be observed in the B-factors of the crystal structures 6M17 (WT complex) and 7WBP (Omicron complex); the WT interface backbone shows a moderate 3.9% increase in the median B-factor with respect to the median B-factor of the whole backbone, while the Omicron interface backbone median B-factor decreases by 21.5%.

5. DISCUSSION

In this study, we analyzed the behavior of the fully glycosylated S-RBD:ACE2 complex both in the case of the WT and the Omicron structure via MD simulations. We found several structural and dynamical changes of high significance. The overall electrostatic distribution of the S-RBD surface is decidedly more positive in the case of the Omicron variant, which can help the virus to identify the predominantly negatively charged ACE2 interface and initialize the ACE2 binding process. However, our results indicate that the resulting Omicron S-RBD:ACE2 complex will not be more stable than the WT complex, especially because the reduction of flexibility of surface loops of the S-RBD is also unfavorable via the entropic term.

Experimental evaluation of the affinity of the Omicron variant toward ACE2 remains surprisingly eluding, different methods deriving strikingly contrasting results, ranging from a decided increase to significant reduction as compared to that of the WT.[17,24−28] Previous theoretical studies overwhelmingly predicted stronger association between the RBD of the Omicron variant and ACE2,[49−53] based on calculated binding energies without the analysis of the dynamic properties of the complex. Deep mutational scanning results[54] indicate near unchanged binding potential for the Omicron variant: the N440K, S477N, and N501Y single mutations increased and S375F, K417N, G496S, and Y505H changes decreased, while the other Omicron mutations (introduced one-by-one) did not exert a significant effect on ACE2 binding efficiency. Thus, we can conclude that the drastically increased infectivity and quick spread of the Omicron variant cannot be explained (at least not alone) through more optimal binding with the ACE2.

In the Omicron variant, besides those of the RBD domain, mutations appear both in the inner architecture of the tightly packed S2 helices and also in the vicinity of the S1/S2 proteolysis site: H655Y in spatial proximity, N679K next to the O-glycosylated[55] T^{678} and P681H directly preceding the polybasic -RRAR- (residues 682−685) recognition motif of the furin cleavage site, that prompts the first proteolysis (of the R^{685}-S^{686} peptide bond) of the activation cascade of the Spike protein. These changes have the capacity of altering the flexibility and accessibility of this site, which results in reduced effectiveness of the cleavage,[16,17] but could also alter the affinity of the spike protein toward neuropilin-1 receptors that also bind to this specific motif. Neuropilin-1 receptors are abundant in the respiratory and nasal passages most easily accessed by the virus and are shown to potentiate ACE2-mediated cell entry as well as functioning as possible independent receptors for SARS-CoV-2 viruses.[56,57] It is tempting to speculate that the greater transmissibility of the Omicron variant could—at least partially—be explained by enhanced interaction with neuropilin-1 receptors due to the mutations near the S1/S2 proteolysis site. Alternatively, it seems the Omicron variant might also use the endosomal pathway for host cell entry, as suggested by a recent study.[19] Either way, the picture that emerges, based also on our results, is that while the Omicron mutations improve the overall electrostatic complementarity of the S-RBD and the human ACE2 receptor, the optimized residue−residue contacts especially in the middle of the interaction surface result in an unfavorably rigidified complex, thus the fast spread and great infectivity of the Omicron SARS-CoV-2 virus cannot be attributed to this interaction. The conflicting aspects of the binding process between the S-RBD and ACE2 that we uncovered might explain the differing experimental results concerning the affinity of the two and also suggest that mutations in the Patch II region of S-RBD (residues 493−505) that do not participate in antibody binding might recover the virus's affinity toward human ACE2 without the loss of its evasion mechanism, producing both a highly infectious and severe variant.

MATERIALS AND METHODS

For MD simulations, the 6M17 PDB was used as a starting structure. Glycan modifications were built on ACE2 at residues N^{53}, N^{90}, N^{103}, N^{322}, N^{432}, and N^{546}, while on the RBD at N^{343} using the most abundant glycan-modifications published.[47] The globular domain of ACE2 is built from two relatively rigid lobes that maintain an open conformation in the *apo* state, but close upon the physiological substrates of the enzyme[58] when they are bound to the active site. The architecture of the lobes is organized around ion-binding sites: a Zn^{2+}-ion in the lobe also containing the S-RBD binding surface and a Cl^{-}-ion in center of the other. Both ions are required for efficient catalysis.[59] The structural chloride ion is coordinated by residues W^{165}, R^{169}, W^{478}, K^{481}, and D^{499}, while the zinc ion is clamped by H^{374}, E^{375}, H^{378}, and E^{402}. In the case of the zinc ion (Zn^{2+}), a harmonic potential for the H^{374}:Nε2−Zn bond and the H^{378}:Nε2−Zn bond was applied with an equilibrium bond length of 0.229 nm and a force constant of 22,000 kJ·

https://doi.org/10.1021/acs.jcim.2c00397
J. Chem. Inf. Model. XXXX, XXX, XXX−XXX

$mol^{-1}·nm^{-2}$. The H^{374}:Nε2−Zn−H^{378}:Nε2 angle was also penalized[60] with a harmonic potential with an equilibrium angle of 88.4° and a force constant of 60 $kJ·mol^{-1}·nm^{-2}$. The structure for the Omicron variant RBD was constructed from the above PDB file, using the Schrödinger Maestro 2022.1 software. The MD simulations were carried out by using the GROMACS 2021.4 software.[61−63] The proteins were solvated in water with an OPC water model,[64] and sodium and chloride ions were added to electrostatically neutralize the system, at a final concentration of 0.15 M. The forcefield employed here was AMBER-ff99SBildnp-star.[65] Parameters, that is, force constants and equilibrium bond lengths and angles for the glycan modifications were based on the existing RNA sugar parametrizations of the force-field, while partial charges were calculated from B3LYP/6-31G** optimized wave functions of the sugar units, using the electrostatic potential-fitted charge calculation protocol (ESP charges) [using Jaguar[66] of the Schrödinger Suite (Schrödinger, LLC, New York, NY 2021)]. Before the production MD, several equilibration steps were performed; first, using a steepest descent integrator with position restraints of 1000, 500, 100, and then 0 $kJ·mol^{-1}·nm^{-2}$ and a maximal force tolerance of 50 $kJ·mol^{-1}·nm^{-1}$. Next, an NVT equilibration was performed using the leap-frog integrator for 50,000 steps with a 2 fs step-size with position restraints of 1000, 500, 100, and 0 $kJ·mol^{-1}·nm^{-2}$ again at 310 K. Finally, an unconstrained NPT step was included to allow introduction of pressure. From the starting structures, thus obtained 2000 ns production runs were started. In the case of the Omicron S-RBD:ACE2 complex, two independent runs were produced to make our analyses more robust against the initial conditions.

For the investigation of the residue−residue contacts in both the WT and Omicron complexes, we first clustered the extended contact group of the interaction surface, comprised of residues 21−52, 76−84, 315−326, 348−358, and 382−394 in ACE2, and 403−506 of S-RBD, using the *gmx cluster* command with the *gromos* method and a distance cutoff of 1.5 Å. The cluster centers of these clusters served as representative structures for further comprehensive investigations. To compare the interface structures, we created LigPlots[67] representing the measured WT S-RBD:ACE2 interface (Figure S2/A), the measured Omicron S-RBD:ACE2 interface (Figure S2/B), and also the cluster centers of their simulated counterparts (Figures S3 and S4). We also collected the main contact partners for the residues at the mutation sites in both the WT and the Omicron complex. More precisely, at a given snapshot, we call a residue R_c contacting with a residue R_m at the mutation site, if any of R_c's atoms is closer to R_m than 4 Å. Then, we only considered R_cs that contacted with R_m for more than 15% of the time along the trajectory. For these residues, we measured the distances between atoms that can potentially participate in residue−residue interactions, like H-bonds, salt bridges, and aromatic interactions. These distance measurements were only kept, if they were closer than 3.5 Å for more than 15% of the time along the trajectory. The histograms for these measurements are collected in Figures S5−S11. The SpR values were calculated using these distances with the 1.7.1 version of scipy in Python 3.8. This way, the time-sorted ranks of the distance−value pairs were correlated, which is independent of the linearity/non-linearity of their relationship and only depends on the monotonicity of the change.

When considering the effects of the glycan modifications, it is important to keep in mind that the chosen glycans are samples from a larger distribution. The conditions we applied for selecting a glycan−residue contact were equivalent to that used in the case of residue−residue contacts, that is, the residue must be closer than 4.0 Å to the corresponding glycan for more than 15% of the full analyzed trajectory time.

PCA analysis of the trajectories was carried out using the *gmx covar* and *gmx anaeig* built-in functions of GROMACS on the MainChain + Cβ atom groups. We analyzed three converged 500 ns length trajectory slices, one from the WT trajectory, and two from the two Omicron trajectories. In order to visualize the movement of the proteins along these *eigen*-axes, for each *eigen*-axis we extracted the two structures along the trajectory, for which the coordinate along the given axis is maximal and minimal. Then, we visualized the transition from one structure to the other using linear interpolation.

For the rigid body segmentation, the scikit-learn 1.0.1, numpy 1.20.3, and mdanalysis 2.0.0[68] Python 3.8 compatible packages were used. For each frame, the Cα-Cα Euclidean distance matrix was constructed, then the Welford online algorithm was used for the calculation of the standard deviation matrix. This matrix was provided as a precomputed metric to the DBSCAN algorithm. In both cases (for the WT and the Omicron complex) we used an epsilon value of 0.2 nm and a min_samples value of five in the DBSCAN algorithm. The same trajectory slices were used for the rigid body segmentation algorithm as for the PCA.

Binding energy was estimated using the PISA server[69,70] to calculate a cluster weighted average of $\Delta_{bind}G$ (cluster midstructures were evaluated with PISA and considered with the weight derived from the population ratio of the given cluster). In the case of the WT complex, the first seven cluster mid-structures were used with a total population coverage of 75%, while in the case of the Omicron complex we used five clusters with 78% coverage.

ABPS[71] surfaces and molecular visualizations were made using the PyMOL Molecular Graphics System, Version 2.0 Schrödinger, LLC.

DATA AND SOFTWARE AVAILABILITY

Additional data, that is, results of trajectory clustering, results of scripts, as well as usage of the rigid body segmentation, and movies depicting the movements along the eigen axes are available (see Supporting Information).

ASSOCIATED CONTENT

Supporting Information

The Supporting Information is available free of charge at https://pubs.acs.org/doi/10.1021/acs.jcim.2c00397.

Graph of the evolution of RMSD and SASA; LigPlots of the experimentally determined interfaces; LigPlots of the cluster centers for the WT complex simulation; LigPlots of the cluster centers for the Omicron mutant complex simulation; residue-specific interactions; interface electrostatics; glycan-specific interactions; distribution of the number of H-bonds; and schematics for the complex movement along the principal axes (PDF)

GIF animations, representing the movement along the principal axes; PDB files, containing the cluster centers and rigid body segmentation results (as B-factor labels);

https://doi.org/10.1021/acs.jcim.2c00397
J. Chem. Inf. Model. XXXX, XXX, XXX−XXX

the rigid body segmentation Python script and its usage in a simple text file (ZIP)

AUTHOR INFORMATION

Corresponding Author

András Perczel − *Laboratory of Structural Chemistry and Biology, Institute of Chemistry and MTA-ELTE Protein Modeling Research Group, Eötvös Loránd Research Network (ELKH), ELTE Eötvös Loránd University, Budapest 1117, Hungary;* orcid.org/0000-0003-1252-6416; Email: perczel.andras@ttk.elte.hu

Authors

Zsolt Fazekas − *Laboratory of Structural Chemistry and Biology, Institute of Chemistry and ELTE Hevesy György PhD School of Chemistry, ELTE Eötvös Loránd University, Budapest 1117, Hungary;* orcid.org/0000-0001-5007-4807

Dóra K. Menyhárd − *Laboratory of Structural Chemistry and Biology, Institute of Chemistry and MTA-ELTE Protein Modeling Research Group, Eötvös Loránd Research Network (ELKH), ELTE Eötvös Loránd University, Budapest 1117, Hungary;* orcid.org/0000-0002-0095-5531

Complete contact information is available at: https://pubs.acs.org/10.1021/acs.jcim.2c00397

Notes

The authors declare no competing financial interest.

ACKNOWLEDGMENTS

This work was supported by project no. 2018-1.2.1-NKP-2018-00005 (HunProtExc) of the National Research Development and Innovation Fund of Hungary; no. VEKOP-2.3.2-16-2017-00014 and VEKOP-2.3.3-15-2017-00018 of the European Union and the State of Hungary, cofinanced by the European Regional Development Fund; by MedInProt Grants from the Hungarian Academy of Sciences; and within the framework of the Thematic Excellence Program 2019 by the National Research, Development and Innovation Office under project "Szint+" as well as the Hungarian Scientific Research Fund (NKFIH-OTKA).

REFERENCES

(1) New York State. *Novel Coronavirus*; COVID-19 Variant Data. https://coronavirus.health.ny.gov/covid-19-variant-data (accessed Feb 02, 2022).

(2) Venkatakrishnan, A.; Anand, P.; Lenehan, P.; Suratekar, R.; Raghunathan, B.; Niesen, M. J. M.; Soundararajan, V. Omicron variant of SARS-CoV-2 harbors a unique insertion mutation of putative viral or human genomic origin. *Omicron Variant of SARS-CoV-2 Harbors a Unique Insertion Mutation of Putative Viral or Human Genomic Origin; Preprint*; Open Science Framework, 2021.

(3) Stanford Univerity. Coronavirus Antiviral & Resistance Database. https://covdb.stanford.edu/page/mutation-viewer/(accessed Feb 02, 2022).

(4) Zhang, H.; Penninger, J. M.; Li, Y.; Zhong, N.; Slutsky, A. S. Angiotensin-Converting Enzyme 2 (ACE2) as a SARS-CoV-2 Receptor: Molecular Mechanisms and Potential Therapeutic Target. *Intensive Care Med.* **2020**, *46*, 586−590.

(5) Jackson, C. B.; Farzan, M.; Chen, B.; Choe, H. Mechanisms of SARS-CoV-2 Entry into Cells. *Nat. Rev. Mol. Cell Biol.* **2022**, *23*, 3−20.

(6) Hussain, M.; Jabeen, N.; Raza, F.; Shabbir, S.; Baig, A. A.; Amanullah, A.; Aziz, B. Structural variations in human ACE2 may influence its binding with SARS-CoV-2 spike protein. *J. Med. Virol.* **2020**, *92*, 1580−1586.

(7) Chen, J.; Malone, B.; Llewellyn, E.; Grasso, M.; Shelton, P. M. M.; Olinares, P. D. B.; Maruthi, K.; Eng, E. T.; Vatandaslar, H.; Chait, B. T.; Kapoor, T. M.; Darst, S. A.; Campbell, E. A. Structural Basis for Helicase-Polymerase Coupling in the SARS-CoV-2 Replication-Transcription Complex. *Cell* **2020**, *182*, 1560−1573.

(8) Yan, L.; Zhang, Y.; Ge, J.; Zheng, L.; Gao, Y.; Wang, T.; Jia, Z.; Wang, H.; Huang, Y.; Li, M.; Wang, Q.; Rao, Z.; Lou, Z. Architecture of a SARS-CoV-2 Mini Replication and Transcription Complex. *Nat. Commun.* **2020**, *11*, 5874.

(9) Ye, Q.; West, A. M. V.; Silletti, S.; Corbett, K. D. Architecture and self-assembly of the SARS-CoV -2 nucleocapsid protein. *Protein Sci.* **2020**, *29*, 1890−1901.

(10) Mendonça, L.; Howe, A.; Gilchrist, J. B.; Sheng, Y.; Sun, D.; Knight, M. L.; Zanetti-Domingues, L. C.; Bateman, B.; Krebs, A.-S.; Chen, L.; Radecke, J.; Li, V. D.; Ni, T.; Kounatidis, I.; Koronfel, M. A.; Szynkiewicz, M.; Harkiolaki, M.; Martin-Fernandez, M. L.; James, W.; Zhang, P. Correlative Multi-Scale Cryo-Imaging Unveils SARS-CoV-2 Assembly and Egress. *Nat. Commun.* **2021**, *12*, 4629.

(11) Chen, D.; Zheng, Q.; Sun, L.; Ji, M.; Li, Y.; Deng, H.; Zhang, H. ORF3a of SARS-CoV-2 Promotes Lysosomal Exocytosis-Mediated Viral Egress. *Dev. Cell* **2021**, *56*, 3250−3263.

(12) Aine, O.; Hill, V. *CoV-Lineages*; Cov-lineages. https://cov-lineages.org/global_report_B.1.1.7.html (accessed Feb 02, 2022).

(13) Vaughan, A. Delta to Dominate World. *New Sci.* **2021**, *250*, 9.

(14) Hodcroft, E. *CoVariants*; covariants. https://covariants.org/per-country (accessed Feb 02, 2022).

(15) Centers for Disease Control and Prevention. https://covid.cdc.gov/covid-data-tracker/#variant-proportions (accessed Feb 02, 2022).

(16) Meng, B.; Abdullahi, I. A. T. M.; Ferreira, A.; Goonawardane, N.; Saito, A.; Kimura, I.; Yamasoba, D.; Gerber, P. P.; Fatihi, S.; Rathore, S.; Zepeda, S. K.; Papa, G.; Kemp, S. A.; Ikeda, T.; Toyoda, M.; Tan, T. S.; Kuramochi, J.; Mitsunaga, S.; Ueno, T.; Shirakawa, K.; Takaori-Kondo, A.; Brevini, T.; Mallery, D. L.; Charles, O. J.; Baker, J. E.; Dougan, A.; Hess, A. C.; Kingston, L.; Lehner, S.; Lyons, D.; Matheson, K. G. C.; Ouwehand, J.; Saunders, J. A. G.; Summers, J.; Thaventhiran, E.; Toshner, K.; Weekes, P.; Maxwell, L.; Shaw, R.; Bucke, S.; Calder, M.; Canna, A.; Domingo, D.; Elmer, A.; Fuller, L.; Harris, D.; Hewitt, M.; Kennet, J. H.; Jose, F.; Kourampa, I. G.; Meadows, N. J.; O'Brien, L.; Price, K.; Publico, R. K.; Rastall, R.; Ribeiro, C.; Rowlands, J.; Ruffolo, V.; Tordesillas, H.; Bullman, B.; Dunmore, B. J.; Gräf, S.; Hodgson, J.; Huang, C.; Hunter, K.; Jones, E.; Legchenko, E.; Matara, C.; Martin, J.; Mescia, F.; O'Donnell, C.; Pointon, L.; Shih, J.; Sutcliffe, R.; Tilly, T.; Treacy, C.; Tong, Z.; Wood, J.; Wylot, M.; Betancourt, A.; Bower, G.; Cossetti, C.; De Sa, A.; Epping, M.; Fawke, S.; Gleadall, N.; Grenfell, R.; Hinch, A.; Jackson, S.; Jarvis, I.; Krishna, B.; Nice, F.; Omarjee, O.; Perera, M.; Potts, M.; Richoz, N.; Romashova, V.; Stefanucci, L.; Strezlecki, M.; Turner, L.; De Bie, E. M. D. D.; Bunclark, K.; Josipovic, M.; Mackay, M.; Butcher, H.; Caputo, D.; Chandler, M.; Chinnery, P.; Clapham-Riley, D.; Dewhurst, E.; Fernandez, C.; Furlong, A.; Graves, B.; Gray, J.; Hein, S.; Ivers, T.; Le Gresley, E.; Linger, R.; Kasanicki, M.; King, R.; Kingston, N.; Meloy, S.; Moulton, A.; Muldoon, F.; Ovington, N.; Papadia, S.; Penkett, C. J.; Phelan, I.; Ranganath, V.; Paraschiv, R.; Sage, A.; Sambrook, J.; Scholtes, I.; Schon, K.; Stark, H.; Stirrups, K. E.; Townsend, P.; Walker, N.; Webster, J.; Butlertanaka, E. P.; Tanaka, Y. L.; Ito, J.; Uriu, K.; Kosugi, Y.; Suganami, M.; Oide, A.; Yokoyama, M.; Chiba, M.; Motozono, C.; Nasser, H.; Shimizu, R.; Kitazato, K.; Hasebe, H.; Irie, T.; Nakagawa, S.; Wu, J.; Takahashi, M.; Fukuhara, T.; Shimizu, K.; Tsushima, K.; Kubo, H.; Kazuma, Y.; Nomura, R.; Horisawa, Y.; Nagata, K.; Kawai, Y.; Yanagida, Y.; Tashiro, Y.; Tokunaga, K.; Ozono, S.; Kawabata, R.; Morizako, N.; Sadamasu, K.; Asakura, H.; Nagashima, M.; Yoshimura, K.; Cárdenas, P.; Muñoz, E.; Barragan, V.; Márquez, S.; Prado-Vivar, B.; Becerra-Wong, M.; Caravajal, M.; Trueba, G.; Rojas-Silva, P.; Grunauer, M.; Gutierrez, B.; Guadalupe, J. J.; Fernández-Cadena, J. C.; Andrade-Molina, D.; Baldeon, M.; Pinos, A.; Bowen, J. E.; Joshi, A.; Walls, A. C.; Jackson, L.; Martin, D.; Smith, K. G. C.; Bradley, J.; Briggs, J. A.

G.; Choi, J.; Madissoon, E.; Meyer, K. B.; Mlcochova, P.; Ceron-Gutierrez, L.; Doffinger, R.; Teichmann, S. A.; Fisher, A. J.; Pizzuto, M. S.; de Marco, A.; Corti, D.; Hosmillo, M.; Lee, J. H.; James, L. C.; Thukral, L.; Veesler, D.; Sigal, A.; Sampaziotis, F.; Goodfellow, I. G.; Matheson, N. J.; Sato, K.; Gupta, R. K. Altered TMPRSS2 Usage by SARS-CoV-2 Omicron Impacts Infectivity and Fusogenicity. *Nature* **2022**, *603*, 706−714.

(17) Zeng, C.; Evans, J. P.; Qu, P.; Faraone, J.; Zheng, Y.-M.; Carlin, C.; Bednash, J. S.; Zhou, T.; Lozanski, G.; Mallampalli, R.; Saif, L. J.; Oltz, E. M.; Mohler, P.; Xu, K.; Gumina, R. J.; Liu, S.-L. Neutralization and Stability of SARS-CoV-2 Omicron Variant. **2021**, 2021.12.16.472934 preprint.

(18) Hui, K. P. Y.; Ho, J. C. W.; Cheung, M.-c.; Ng, K.-c.; Ching, R. H. H.; Lai, K.-l.; Kam, T. T.; Gu, H.; Sit, K.-Y.; Hsin, M. K. Y.; Au, T. W. K.; Poon, L. L. M.; Peiris, M.; Nicholls, J. M.; Chan, M. C. W. SARS-CoV-2 Omicron variant replication in human bronchus and lung ex vivo. *Nature* **2022**, *603*, 715−720.

(19) Peacock, T. P.; Brown, J. C.; Zhou, J.; Thakur, N.; Sukhova, J.; Newman, R.; Kugathasan, K.; Yan, M.; Furnon, D.; De Lorenzo, W. S. The altered entry pathway and antigenic distance of the SARS-CoV-2 Omicron variant map to separate domains of spike protein. **2022**. 10.1101/2021.12.31.474653 Preprint.

(20) Lewnard, J. A.; Hong, V. X.; Patel, M. M.; Kahn, R.; Lipsitch, M.; Tartof, S. Y. Clinical Outcomes Associated with SARS-CoV-2 Omicron (B.1.1.529) Variant and BA.1/BA.1.1 or BA.2 Subvariant Infection in Southern California. *Nat. Med.* **2022**, DOI: 10.1038/s41591-022-01887-z.

(21) Shang, J.; Wan, Y.; Luo, C.; Ye, G.; Geng, Q.; Auerbach, A.; Li, F. Cell Entry Mechanisms of SARS-CoV-2. *Proc. Natl. Acad. Sci. U.S.A.* **2020**, *117*, 11727−11734.

(22) Yang, J.; Petitjean, S. J. L.; Koehler, M.; Zhang, Q.; Dumitru, A. C.; Chen, W.; Derclaye, S.; Vincent, S. P.; Soumillion, P.; Alsteens, D. Molecular Interaction and Inhibition of SARS-CoV-2 Binding to the ACE2 Receptor. *Nat. Commun.* **2020**, *11*, 4541.

(23) Ni, W.; Yang, X.; Yang, D.; Bao, J.; Li, R.; Xiao, Y.; Hou, C.; Wang, H.; Liu, J.; Yang, D.; Xu, Y.; Cao, Z.; Gao, Z. Role of Angiotensin-Converting Enzyme 2 (ACE2) in COVID-19. *Crit. Care* **2020**, *24*, 422.

(24) Hong, Q.; Han, W.; Li, J.; Xu, S.; Wang, Y.; Xu, C.; Li, Z.; Wang, Y.; Zhang, C.; Huang, Z.; Cong, Y. Molecular basis of receptor binding and antibody neutralization of Omicron. *Nature* **2022**, *604*, 546−552.

(25) Wu, L.; Zhou, L.; Mo, M.; Liu, T.; Wu, C.; Gong, C.; Lu, K.; Gong, L.; Zhu, W.; Xu, Z. SARS-CoV-2 Omicron RBD Shows Weaker Binding Affinity than the Currently Dominant Delta Variant to Human ACE2. *Signal Transduction Targeted Ther.* **2022**, *7*, 8.

(26) Mannar, D.; Saville, J. W.; Zhu, X.; Srivastava, S. S.; Berezuk, A. M.; Tuttle, K. S.; Marquez, C.; Sekirov, I.; Subramaniam, S. SARS-CoV-2 Omicron variant: Antibody evasion and cryo-EM structure of spike protein−ACE2 complex. *Science* **2022**, *375*, 760−764.

(27) Han, P.; Li, L.; Liu, S.; Wang, Q.; Zhang, D.; Xu, Z.; Han, P.; Li, X.; Peng, Q.; Su, C.; Huang, B.; Li, D.; Zhang, R.; Tian, M.; Fu, L.; Gao, Y.; Zhao, X.; Liu, K.; Qi, J.; Gao, G. F.; Wang, P. Receptor Binding and Complex Structures of Human ACE2 to Spike RBD from Omicron and Delta SARS-CoV-2. *Cell* **2022**, *185*, 630.

(28) Cameroni, E.; Bowen, J. E.; Rosen, L. E.; Saliba, C.; Zepeda, S. K.; Culap, K.; Pinto, D.; VanBlargan, L. A.; De Marco, A.; di Iulio, J.; Zatta, F.; Kaiser, H.; Noack, J.; Farhat, N.; Czudnochowski, N.; Havenar-Daughton, C.; Sprouse, K. R.; Dillen, J. R.; Powell, A. E.; Chen, A.; Maher, C.; Yin, L.; Sun, D.; Soriaga, L.; Bassi, J.; Silacci-Fregni, C.; Gustafsson, C.; Franko, N. M.; Logue, J.; Iqbal, N. T.; Mazzitelli, I.; Geffner, J.; Grifantini, R.; Chu, H.; Gori, A.; Riva, A.; Giannini, O.; Ceschi, A.; Ferrari, P.; Cippà, P. E.; Franzetti-Pellanda, A.; Garzoni, C.; Halfmann, P. J.; Kawaoka, Y.; Hebner, C.; Purcell, L. A.; Piccoli, L.; Pizzuto, M. S.; Walls, A. C.; Diamond, M. S.; Telenti, A.; Virgin, H. W.; Lanzavecchia, A.; Snell, G.; Veesler, D.; Corti, D. Broadly Neutralizing Antibodies Overcome SARS-CoV-2 Omicron Antigenic Shift. *Nature* **2022**, *602*, 664.

(29) Lan, J.; Ge, J.; Yu, J.; Shan, S.; Zhou, H.; Fan, S.; Zhang, Q.; Shi, X.; Wang, Q.; Zhang, L.; Wang, X. Structure of the SARS-CoV-2 Spike Receptor-Binding Domain Bound to the ACE2 Receptor. *Nature* **2020**, *581*, 215−220.

(30) Yan, R.; Zhang, Y.; Li, Y.; Xia, L.; Guo, Y.; Zhou, Q. Structural Basis for the Recognition of SARS-CoV-2 by Full-Length Human ACE2. *Science* **2020**, *367*, 1444−1448.

(31) Ali, A.; Vijayan, R. Dynamics of the ACE2-SARS-CoV-2/SARS-CoV spike protein interface reveal unique mechanisms. *Sci. Rep.* **2020**, *10*, 14214.

(32) Shang, J.; Ye, G.; Shi, K.; Wan, Y.; Luo, C.; Aihara, H.; Geng, Q.; Auerbach, A.; Li, F. Structural Basis of Receptor Recognition by SARS-CoV-2. *Nature* **2020**, *581*, 221−224.

(33) Yin, W.; Xu, Y.; Xu, P.; Cao, X.; Wu, C.; Gu, C.; He, X.; Wang, X.; Huang, S.; Yuan, Q.; Wu, K.; Hu, W.; Huang, Z.; Liu, J.; Wang, Z.; Jia, F.; Xia, K.; Liu, P.; Wang, X.; Song, B.; Zheng, J.; Jiang, H.; Cheng, X.; Jiang, Y.; Deng, S.-J.; Xu, H. E. Structures of the Omicron spike trimer with ACE2 and an anti-Omicron antibody: mechanisms for the high infectivity, immune evasion and antibody drug discovery. *Science* **2022**, *375*, 1048.

(34) Tian, W.; Li, D.; Zhang, N.; Bai, G.; Yuan, K.; Xiao, H.; Gao, F.; Chen, Y.; Wong, C. C. L.; Gao, G. F. O-glycosylation pattern of the SARS-CoV-2 spike protein reveals an "O-Follow-N" rule. *Cell Res.* **2021**, *31*, 1123−1125.

(35) Harbison, A. M.; Fogarty, C. A.; Phung, T. K.; Satheesan, A.; Schulz, B. L.; Fadda, E. Fine-Tuning the Spike: Role of the Nature and Topology of the Glycan Shield in the Structure and Dynamics of the SARS-CoV-2 S. *Chem. Sci.* **2022**, *13*, 386−395.

(36) Sztain, T.; Ahn, S.-H.; Bogetti, A. T.; Casalino, L.; Goldsmith, J. A.; Seitz, E.; McCool, R. S.; Kearns, F. L.; Acosta-Reyes, F.; Maji, S.; Mashayekhi, G.; McCammon, J. A.; Ourmazd, A.; Frank, J.; McLellan, J. S.; Chong, L. T.; Amaro, R. E. A Glycan Gate Controls Opening of the SARS-CoV-2 Spike Protein. *Nat. Chem.* **2021**, *13*, 963−968.

(37) Casalino, L.; Gaieb, Z.; Goldsmith, J. A.; Hjorth, C. K.; Dommer, A. C.; Harbison, A. M.; Fogarty, C. A.; Barros, E. P.; Taylor, B. C.; McLellan, J. S.; Fadda, E.; Amaro, R. E. Beyond Shielding: The Roles of Glycans in the SARS-CoV-2 Spike Protein. *ACS Cent. Sci.* **2020**, *6*, 1722−1734.

(38) Mehdipour, A. R.; Hummer, G. Dual Nature of Human ACE2 Glycosylation in Binding to SARS-CoV-2 Spike. *Proc. Natl. Acad. Sci. U.S.A.* **2021**, *118*, No. e2100425118.

(39) Moss, D. L.; Rappaport, J. SARS-CoV-2 Beta Variant Substitutions Alter Spike Glycoprotein Receptor Binding Domain Structure and Stability. *J. Biol. Chem.* **2021**, *297*, 101371.

(40) Luan, B.; Huynh, T. Insights into SARS-CoV-2's Mutations for Evading Human Antibodies: Sacrifice and Survival. *J. Med. Chem.* **2022**, *65*, 2820−2826.

(41) Valério, M.; Borges-Araújo, L.; Melo, M. N.; Lousa, D.; Soares, C. M. SARS-CoV-2 Variants Impact RBD Conformational Dynamics and ACE2 Accessibility. **2021**, 10.1101/2021.11.30.470470 Preprint.

(42) Goher, S. S.; Ali, F.; Amin, M. The Delta Variant Mutations in the Receptor Binding Domain of SARS-CoV-2 Show Enhanced Electrostatic Interactions with the ACE2. *Med. Drug Discovery* **2022**, *13*, 100114.

(43) Ali, F.; Kasry, A.; Amin, M. The New SARS-CoV-2 Strain Shows a Stronger Binding Affinity to ACE2 Due to N501Y Mutant. *Med. Drug Discovery* **2021**, *10*, 100086.

(44) Zhu, X.; Mannar, D.; Srivastava, S. S.; Berezuk, A. M.; Demers, J.-P.; Saville, J. W.; Leopold, K.; Li, W.; Dimitrov, D. S.; Tuttle, K. S.; Zhou, S.; Chittori, S.; Subramaniam, S. Cryo-Electron Microscopy Structures of the N501Y SARS-CoV-2 Spike Protein in Complex with ACE2 and 2 Potent Neutralizing Antibodies. *PLoS Biol.* **2021**, *19*, No. e3001237.

(45) Khan, A.; Zia, T.; Suleman, M.; Khan, T.; Ali, S. S.; Abbasi, A. A.; Mohammad, A.; Wei, D. Higher infectivity of the SARS-CoV-2 new variants is associated with K417N/T, E484K, and N501Y mutants: An insight from structural data. *J. Cell. Physiol.* **2021**, *236*, 7045−7057.

https://doi.org/10.1021/acs.jcim.2c00397
J. Chem. Inf. Model. XXXX, XXX, XXX−XXX

(46) Yang, T.-J.; Yu, P.-Y.; Chang, Y.-C.; Liang, K.-H.; Tso, H.-C.; Ho, M.-R.; Chen, W.-Y.; Lin, H.-T.; Wu, H.-C.; Hsu, S.-T. D. Impacts on the Structure-Function Relationship of SARS-CoV-2 Spike by B.1.1.7 Mutations. **2021**, 10.1101/2021.05.11.443686 Preprint.
(47) Zhao, P.; Praissman, J. L.; Grant, O. C.; Cai, Y.; Xiao, T.; Rosenbalm, K. E.; Aoki, K.; Kellman, B. P.; Bridger, R.; Barouch, D. H.; Brindley, M. A.; Lewis, N. E.; Tiemeyer, M.; Chen, B.; Woods, R. J.; Wells, L. Virus-Receptor Interactions of Glycosylated SARS-CoV-2 Spike and Human ACE2 Receptor. *Cell Host Microbe* **2020**, *28*, 586−601.
(48) Ester, M.; Kriegel, H.-P.; Sander, J.; Xu, X. *A Density-Based Algorithm for Discovering Clusters in Large Spatial Databases with Noise*; KDD-96 Proc., 1996; pp 226−231.
(49) Rath, S. L.; Padhi, A. K.; Mandal, N. Scanning the RBD-ACE2 Molecular Interactions in Omicron Variant. *Biochem. Biophys. Res. Commun.* **2022**, *592*, 18−23.
(50) Koley, T.; Kumar, M.; Goswami, A.; Ethayathulla, A. S.; Hariprasad, G. Structural Modeling of Omicron Spike Protein and Its Complex with Human ACE-2 Receptor: Molecular Basis for High Transmissibility of the Virus. *Biochem. Biophys. Res. Commun.* **2022**, *592*, 51−53.
(51) Ortega, J. T.; Jastrzebska, B.; Rangel, H. R. Omicron SARS-CoV-2 Variant Spike Protein Shows an Increased Affinity to the Human ACE2 Receptor: An In Silico Analysis. *Pathogens* **2021**, *11*, 45.
(52) Golcuk, M.; Yildiz, A.; Gur, M. Omicron BA.1 and BA.2 Variants Increase the Interactions of SARS-CoV-2 Spike Glycoprotein with ACE2. **2021**, 10.1101/2021.12.06.471377 Preprint.
(53) Lupala, C. S.; Ye, Y.; Chen, H.; Su, X.-D.; Liu, H. Mutations on RBD of SARS-CoV-2 Omicron Variant Result in Stronger Binding to Human ACE2 Receptor. *Biochem. Biophys. Res. Commun.* **2022**, *590*, 34−41.
(54) Starr, T. N.; Greaney, A. J.; Hilton, S. K.; Ellis, D.; Crawford, K. H. D.; Dingens, A. S.; Navarro, M. J.; Bowen, J. E.; Tortorici, M. A.; Walls, A. C.; King, N. P.; Veesler, D.; Bloom, J. D. Deep Mutational Scanning of SARS-CoV-2 Receptor Binding Domain Reveals Constraints on Folding and ACE2 Binding. *Cell* **2020**, *182*, 1295−1310.
(55) Sanda, M.; Morrison, L.; Goldman, R. N- and O-Glycosylation of the SARS-CoV-2 Spike Protein. *Anal. Chem.* **2021**, *93*, 2003−2009.
(56) Daly, J. L.; Simonetti, B.; Klein, K.; Chen, K.-E.; Williamson, M. K.; Antón-Plágaro, C.; Shoemark, D. K.; Simón-Gracia, L.; Bauer, M.; Hollandi, R.; Greber, U. F.; Horvath, P.; Sessions, R. B.; Helenius, A.; Hiscox, J. A.; Teesalu, T.; Matthews, D. A.; Davidson, A. D.; Collins, B. M.; Cullen, P. J.; Yamauchi, Y. Neuropilin-1 Is a Host Factor for SARS-CoV-2 Infection. *Science* **2020**, *370*, 861−865.
(57) Cantuti-Castelvetri, L.; Ojha, R.; Pedro, L. D.; Djannatian, M.; Franz, J.; Kuivanen, S.; van der Meer, F.; Kallio, K.; Kaya, T.; Anastasina, M.; Smura, T.; Levanov, L.; Szirovicza, L.; Tobi, A.; Kallio-Kokko, H.; Österlund, P.; Joensuu, M.; Meunier, F. A.; Butcher, S. J.; Winkler, M. S.; Mollenhauer, B.; Helenius, A.; Gokce, O.; Teesalu, T.; Hepojoki, J.; Vapalahti, O.; Stadelmann, C.; Balistreri, G.; Simons, M. Neuropilin-1 Facilitates SARS-CoV-2 Cell Entry and Infectivity. *Science* **2020**, *370*, 856−860.
(58) Towler, P.; Staker, B.; Prasad, S. G.; Menon, S.; Tang, J.; Parsons, T.; Ryan, D.; Fisher, M.; Williams, D.; Dales, N. A.; Patane, M. A.; Pantoliano, M. W. ACE2 X-Ray Structures Reveal a Large Hinge-Bending Motion Important for Inhibitor Binding and Catalysis. *J. Biol. Chem.* **2004**, *279*, 17996−18007.
(59) Guy, J. L.; Jackson, R. M.; Jensen, H. A.; Hooper, N. M.; Turner, A. J. Identification of Critical Active-Site Residues in Angiotensin-Converting Enzyme-2 (ACE2) by Site-Directed Mutagenesis. *FEBS J.* **2005**, *272*, 3512−3520.
(60) Yang, W.; Riley, B. T.; Lei, X.; Porebski, B. T.; Kass, I.; Buckle, A. M.; McGowan, S. Generation of AMBER Force Field Parameters for Zinc Centres of M1 and M17 Family Aminopeptidases. *J. Biomol. Struct. Dyn.* **2018**, *36*, 2595−2604.
(61) Lindahl; Abraham; Hess; Spoel, V. D. *GROMACS 2021.4 Manual*; GROMACS, 2021.
(62) Bekker, H.; Berendsen, H. J. C.; Dijkstra, E. J.; Achterop, S.; van Drunen, R.; van der Spoel, D.; Sijbers, A.; Keegstra, H. Gromacs: A Parallel Computer for Molecular Dynamics Simulations. *Phys. Comput.* **1993**, *92*, 252−256.
(63) Abraham, M. J.; Murtola, T.; Schulz, R.; Páll, S.; Smith, J. C.; Hess, B.; Lindahl, E. GROMACS: High Performance Molecular Simulations through Multi-Level Parallelism from Laptops to Supercomputers. *SoftwareX* **2015**, *1−2*, 19−25.
(64) Izadi, S.; Anandakrishnan, R.; Onufriev, A. V. Building Water Models: A Different Approach. *J. Phys. Chem. Lett.* **2014**, *5*, 3863−3871.
(65) Aliev, A. E.; Kulke, M.; Khaneja, H. S.; Chudasama, V.; Sheppard, T. D.; Lanigan, R. M. Motional timescale predictions by molecular dynamics simulations: Case study using proline and hydroxyproline sidechain dynamics. *Proteins: Struct., Funct., Bioinf.* **2014**, *82*, 195−215.
(66) Bochevarov, A. D.; Harder, E.; Hughes, T. F.; Greenwood, J. R.; Braden, D. A.; Philipp, D. M.; Rinaldo, D.; Halls, M. D.; Zhang, J.; Friesner, R. A. Jaguar: A high-performance quantum chemistry software program with strengths in life and materials sciences. *Int. J. Quantum Chem.* **2013**, *113*, 2110−2142.
(67) Laskowski, R. A.; Swindells, M. B. LigPlot+: Multiple Ligand-Protein Interaction Diagrams for Drug Discovery. *J. Chem. Inf. Model.* **2011**, *51*, 2778−2786.
(68) Gowers, R.; Linke, M.; Barnoud, J.; Reddy, T.; Melo, M.; Seyler, S.; Domański, J.; Dotson, D.; Buchoux, S.; Kenney, I.; Beckstein, O. *MDAnalysis: A Python Package for the Rapid Analysis of Molecular Dynamics Simulations*; MDAnalysis: Austin, Texas, 2016; pp 98−105.
(69) Krissinel, E.; Henrick, K. Inference of Macromolecular Assemblies from Crystalline State. *J. Mol. Biol.* **2007**, *372*, 774−797.
(70) EMBL-EBI. *PDBePISA*; EMBL-EBI. http://www.ebi.ac.uk/pdbe/prot_int/pistart.html (accessed Feb 02, 2022).
(71) Jurrus, E.; Engel, D.; Star, K.; Monson, K.; Brandi, J.; Felberg, L. E.; Brookes, D. H.; Wilson, L.; Chen, J.; Liles, K.; Chun, M.; Li, P.; Gohara, D. W.; Dolinsky, T.; Konecny, R.; Koes, D. R.; Nielsen, J. E.; Head-Gordon, T.; Geng, W.; Krasny, R.; Wei, G.; Holst, M. J.; McCammon, J. A.; Baker, N. A. Improvements to the APBS Biomolecular Solvation Software Suite. *Protein Sci.* **2018**, *27*, 112−128.

https://doi.org/10.1021/acs.jcim.2c00397
J. Chem. Inf. Model. XXXX, XXX, XXX−XXX